ACS Partner Journal

CHEMICAL & BIOMEDICAL IMAGING

pubs.acs.org/ChemBioImaging

Article

Unveiling the Local Fate of Charge Carriers in Halide Perovskite Thin Films via Correlation Clustering Imaging

Published as part of Chemical & Biomedical Imaging special issue "Imaging in Energy Science".

Sudipta Seth,* Boris Louis, Koki Asano, Toon Van Roy, Maarten B. J. Roeffaers, Elke Debroye, Ivan G. Scheblykin, Martin Vacha,* and Johan Hofkens*

Cite This: *Chem. Biomed. Imaging* 2025, 3, 244−252

Read Online

ACCESS | Metrics & More | Article Recommendations | Supporting Information

ABSTRACT: As the field of metal halide perovskites matures, a range of compositionally different perovskite films has found a place in efficient optoelectronic devices. These films feature variable local structural stability, carrier diffusion, and recombination, while there is still a lack of easy-to-implement generic protocols for high-throughput characterization of these variable properties. Correlation clustering imaging (CLIM) is a recently developed tool that resolves peculiarities of local photophysics by assessing the dynamics of photoluminescence detected by wide-field optical microscopy. We demonstrate the capability of CLIM as a high-throughput characterization tool of perovskite films using $MAPbI_3$ (MAPI) and triple cation mixed halide (TCMH) perovskites as examples where it resolves the interplay of carrier diffusion, recombination, and defect dynamics. We found significant differences in the appearance of metastable defect states in these two films. Despite a better surface quality and larger grain size, MAPI films showed more pronounced effects of fluctuating defect states than did TCMH films. As CLIM shows a significant difference between materials known to lead to different solar cell efficiencies, it can be considered a tool for quality control of thin films for perovskite optoelectronic devices.

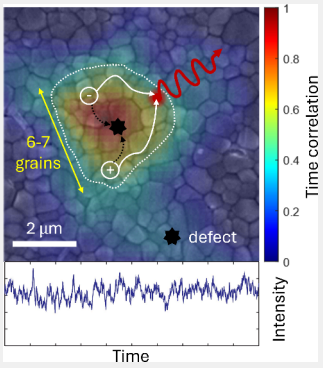

KEYWORDS: *Structure−function relationship, local photophysics, functional imaging, halide perovskites, metastable defects*

INTRODUCTION

Demand for low-cost renewable energy has driven a rapid increase in photovoltaic research. Metal halide perovskites (MHPs) are promising contemporary materials which have been under intense scrutiny for a decade. Impressive power conversion efficiency exceeding 26% in single junction and 33% in tandem solar cell configuration make perovskites a candidate next-generation photovoltaic material.[1] The perovskite films used in these devices are generally prepared in cost-effective ways such as easy solution processable methods at ambient conditions.[2] These thin films consisting of nano- to microscale grains host a significant number of parasitic defect states that trap photogenerated charge carriers and convert their energy to heat/light.[3] Moreover, these traps are often the driver of the degradation of solar cells.[4,5] Thus, the concentration and efficacy of these traps limit the diffusion length and availability of photogenerated charge carriers, adversely affecting the device's efficiency and stability.

Several advanced time-resolved optical spectroscopy techniques, which directly probe the photophysical response of perovskite materials, have shown carrier diffusion lengths ranging from less than a micron to several microns and lifetimes from tens of nanoseconds to microseconds.[6−11] The higher values are typically observed in single crystals rather than films.[7] Most of these techniques are macroscopic and deal with a rather uniform carrier population averaged in space. However, several correlative microscopy studies in polycrystalline perovskite films reveal local structural and compositional disorders.[12] For instance, optical microscopy combined with structural and compositional characterization techniques has been resourceful in understanding different aspects of structure-related optoelectronic response.[13] In addition, correlative electron and photoluminescence (PL) microscopy has shown that PL heterogeneity varies from grain to grain. This depicts an intriguing role of grain boundaries, which sometimes show carrier mobility across the grain and can occasionally act as a blocking layer of charge carriers.[14−18] As the modalities of these microscopy techniques increased, more intricate pictures have emerged. Localization of the performance limiting traps as clusters in grain boundaries,[19,20] anticorrelation of PL with local strain[21] and carrier funneling to the low bandgap nanoscale regions in chemically heterogeneous samples[22] are a few highlights. Therefore,

Received: December 30, 2024
Revised: February 3, 2025
Accepted: February 6, 2025
Published: February 17, 2025

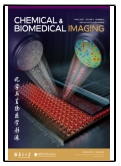

local disorders introducing optoelectronic heterogeneity are a matter of ongoing investigation.

Although PL quenching trap states are often contextualized with spatial heterogeneity and charge carrier dynamics at nano- and microsecond time scales, it is also necessary to consider the real-time behavior of these traps for comprehensive understanding of the materials. In MHPs, it is observed ubiquitously that trap states are dynamic in their configuration frequently transitioning from active (efficient trapping) to inactive (inefficient trapping) states resulting in fluctuation of PL, electroluminescence (EL) and surface photovoltage on scales from microseconds to seconds in time and nanometers to micrometers in space.[23−29] These traps in the active state work as local quenching channels of the excitations (channels of nonradiative recombination of charge carriers) impacting the carrier diffusion and lifetime. To be precise, hereafter, we refer to these traps as nonradiative recombination channels (NRCs). Therefore, mapping changes in PL fluctuation behavior over space will enable landscaping the complex interplay of the carrier generation, diffusion, fast nonradiative and slow radiative recombination, and defect dynamics, thus picturing the features essential for understanding the functionality of MHP films in devices. This can be realized by our recently developed Correlation Clustering Imaging (CLIM), a novel imaging technique based on wide-field microscopy that utilizes spatial variability in temporal PL fluctuations for functional imaging of dynamic semiconductor films[30]

CLIM coupled with electron microscopy can rationalize the relationship between local structure and photophysical property of any dynamic material like MHPs.[30] Here we have implemented the correlative microscopy of CLIM, CLIMSCI (vide infra), and scanning electron microscopy (SEM) to understand the local photophysical response of $MAPbI_3$ (MAPI) and $Cs_{0.05}(MA_{0.14}, FA_{0.86})_{0.95}$ Pb $(I_{0.84}, Br_{0.16})_3$ triple cation mixed halide (TCMH) perovskite thin films. While MAPI is the most studied perovskite composition, TCMH is structurally and thermally more stable with higher power conversion efficiency in corresponding solar cells.[31] From the correlative imaging, we found that both films consist of independent microscale functional domains that consist of several crystal grains. We have semiquantitatively depicted that metastable NRC concentration is high in MAPI as compared to TCMH.

RESULTS

Functional Imaging: Correlation Clustering Imaging (CLIM) and CLIM Extended Spatiotemporal Correlation Decay Imaging (CLIMSCI)

Temporal photoluminescence heterogeneity popularly known as PL blinking is a common phenomenon for most single-photon emitters such as organic molecules and semiconductor quantum dots.[32−37] PL blinking originates from photochemical processes, such as conformational changes and dynamic generation and annihilation of PL quenchers in these systems. These systems with dimensions below 20 nm have been extensively used as blinking labels for super-resolution imaging.[32,38] When many such emitting objects are placed within a diffraction-limited area, the PL of these appear nonfluctuating due to ensemble averaging over many independent single-photon emitters. However, certain micrometer-sized bulk semiconductor materials such as nanoplates, nanorods, nanowires (metal-chalcogenides, MHPs), and grains in thin films (MHPs) show PL fluctuation or blinking despite being essentially multiphoton emitters.[17,39−42] The particular reasons for these fluctuations are system-dependent; generally, they originate from the transport of excited states over space and local photochemical reactions involving defect states. Thus, fluctuations of local PL intensity visualize photochemical/photophysical processes in the material.[33] To understand the space and time-resolved photophysics of these large systems we recently developed Correlation Clustering Imaging (CLIM)[30,43] which we expand further in this report with the Spatiotemporal Correlation Decay Imaging (CLIMSCI) modality.

As input, CLIM utilizes widefield photoluminescence microscopy image stacks (movies) showing local intensity variations in time such as blinking, bleaching, enhancement, or a combination of these. CLIM analyses the correlation (Pearson correlation coefficient[44]) of PL change over time among pixels in local regions to identify spatially synchronous regions of any extent as indicated with variable correlation coefficient. Therefore, the correlation map is the first output of CLIM. Upon implementation of a certain threshold (this stage is sample-specific and automated), one can obtain a cluster map. Here each cluster has a high intracluster correlation and low intercluster correlation. Notably, CLIM does not provide PL fluctuation kinetics as an output. Further intricate details of the CLIM methodology are provided in our previous paper[30,43] and in the Materials and Methods. Generally, the area close to the location of the fluctuating nonradiative recombination channel (NRC, the origin of the fluctuating signal) presents the highest correlation. Over which distance a single fluctuating NRC influences the PL must then depend on the carrier quenching efficiency and diffusion coefficient of the carriers. It is anticipated that the correlation will gradually decrease as the distance increases from the location of the NRC. Therefore, it is quite intuitive to extend CLIM to analyze the decay of correlation as a function of surrounding space for a selected pixel.

To this end, we have developed Spatiotemporal Correlation Decay Imaging (CLIMSCI), which, instead of finding regions of synchronous blinking (as in CLIM), uncovers how the synchronicity of blinking extends in space for a region of interest. The first step of the process is to calculate the CLIM correlation image to visualize the point of interest in the sample (e.g., region of high and low correlation). Then, the user can select the pixels of interest in the image. For each of these pixels, CLIMSCI calculates the correlation in time of that pixel with all of the surrounding pixels within a predefined radius. The correlation of the pixel with itself is always 1. Concerning the surrounding pixels, if there is no correlation (e.g., stable PL signal or background), the correlation instantly decays to a very low value close to zero. However, if the PL fluctuates also around the selected pixel, then there will be a correlation between that pixel and the neighboring ones. CLIMSCI portrays the spatial extent of this correlation which depends on the extent of carrier communication, quenching ability, and presence of additional NRCs in nearby space and can therefore directly report on these phenomena.

Since CLIM and CLIMSCI utilize correlation coefficient analysis of spatiotemporal PL fluctuation, one might find conceptual similarity with previously developed Image Correlation Spectroscopy (ICS).[45,46] Different ICS modalities, including spatiotemporal ICS, use autocorrelation of PL in

https://doi.org/10.1021/cbmi.4c00113
Chem. Biomed. Imaging 2025, 3, 244−252

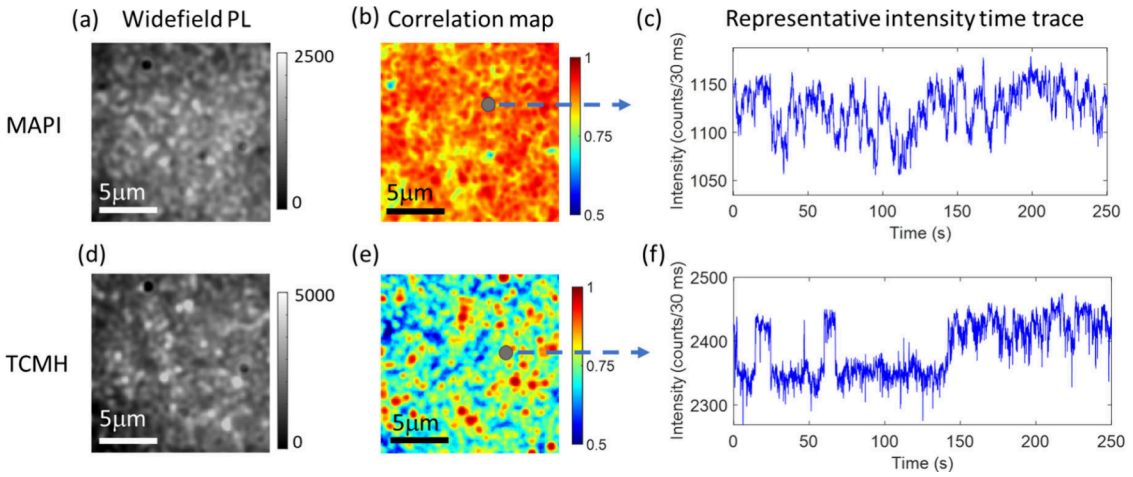

Figure 1. Widefield PL microscopy and CLIM imaging of MAPI (a-c) and TCMH (d-f) thin films. (a,d) Time-averaged PL images obtained from the movies (4000 frames). (b,d) Correlation map of CLIM imaging demonstrating nano to microscale heterogeneity. While high correlation regions dominate the MAPI film, TCMH features mostly low correlation with randomly distributed microscale high correlation regions. (c,f) Representative PL intensity traces extracted from both films' high correlation regions as marked with arrows.

space or time of a region of interest (ROI) in the image. Considering the Gaussian point spread function (PSF) and two-level system of the underlying emitter, the autocorrelation function is further modeled to identify diffusion coefficients, molecular concentrations, or mobility patterns of the system. In semiconductor materials, emitting units larger than the quantum confinement regime—such as grains in a thin film—are typically multiphoton emitters.[42] Since these emitters often exceed the diffraction limit and vary in shape and size, defining them with a generic PSF is challenging. Instead, CLIM and CLIMSCI simplify correlation analysis by leveraging PL fluctuations at the individual pixel level and apply to any large emitter irrespective of their morphological shape and size or point spread function. As PL fluctuations reflect intrinsic photoinduced processes in material systems, CLIM and CLIMSCI are well-suited for material investigations.

We have chosen $MAPbI_3$ (MAPI) and $Cs_{0.05}(MA_{0.14}, FA_{0.86})_{0.95}$ Pb $(I_{0.84}, Br_{0.16})_3$ triple cation mixed halide (TCMH) perovskite thin films, which are two state of the art materials for the present investigation. These films were grown on glass coverslips through simple solution processing following the reported procedure with little modifications (detailed in Materials and Methods).[17,47] No additional coating layers are used to protect the samples from the ambiance. As evident from SEM images, average grain size in MAPI and TCMH is 280 and 150 nm, respectively (Figure S1a,b, Supporting note 1). The thickness of the films is in the range of 150−200 nm (cross-sectional SEM image, Figure S1c,d Supporting note 1). Steady-state absorption and emission suggest a similar band gap of MAPI and TCMH perovskites (Figure S2, Supporting note 2). Steady-state PL measurements carried out at several submicrometer regions of the films reproduce similar emission features (Figure S3, Supporting note 3). This suggests minimal compositional heterogeneity across films.

We have investigated these films in a standard wide-field PL microscope (details are provided at Materials and Methods) at an excitation wavelength of 720 nm of a supercontinuum laser with a power density of 0.7 W/cm^2. PL of the films are collected from the entire emission spectra longer than 740 nm. PL movies were recorded with 30 ms exposure time. The pixel size of the CCD camera is 100 nm. Objective's numerical aperture of 0.95 and emission wavelength at 760 nm results in an estimated diffraction limit of the setup approximately 400 nm. Notably, we observed an initial increase in PL intensity within the first 5−10 min of laser exposure, followed by signal stabilization. Under the specified experimental conditions, photobleaching remains negligible, even after several hours of continuous measurement.

Time averaged PL microscopy imaging (Figure 1a,d) of the perovskite films reveals significant spatial heterogeneity in the submicron scale as typically observed in several other perovskite films.[12,14] However, spatiotemporal PL heterogeneity or PL fluctuation in MAPI and TCMH differs significantly (Supporting Movies 1 and 2). Careful visualization of the movies demonstrates that the local fluctuations are faster and appear spatially everywhere in the MAPI film. However, in TCMH local fluctuations are slower and reside sparsely (Supporting Movies 1, 2). To obtain a quantitative estimation of this local photophysics, we implemented CLIM on both samples. CLIM's correlation map presents a contrasting behavior between the films (Figure 1b, e). While in MAPI a high correlation above 0.75 is observed, in TCMH a lower correlation (0.5−0.7) prevails across the films. Generally, submicrometer-scale high-correlation domains are separated by low-correlation regions. Although high-correlation domains are closely located in MAPI, such regions are usually several micrometers apart in TCMH. Moreover, the signature of the PL fluctuation obtained from the high correlation regions is notably different. While in MAPI, PL traces show mostly flickering (gradual intensity change) without clear intensity levels (Figure 1c), in TCMH, PL frequently jumps between few intensity levels resembling the step-blinking of perovskite nanocrystals (Figure 1f).[23,40] It is, therefore, evident that these two perovskite films are significantly different in their microscopic photophysical responses.

We have shown previously that a single metastable NRC generally introduces sharp transitions between two intensity levels.[23] A few of these NRCs with the same or variable active to passive switching rate introduce multiple intensity levels, causing step blinking. This is likely the scenario in TCMH. However, when several NRCs work on a diffraction-limited

https://doi.org/10.1021/cbmi.4c00113
Chem. Biomed. Imaging 2025, 3, 244−252

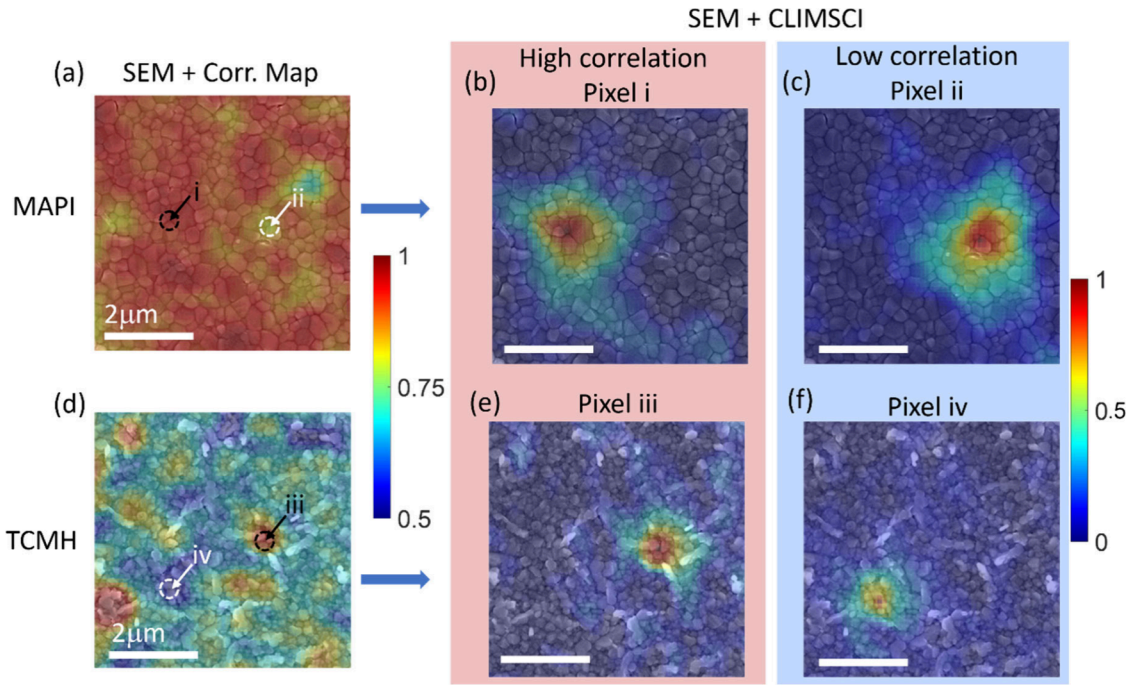

Figure 2. Correlative microscopy analysis employing SEM, CLIM and CLIMSCI. Overlaid SEM image and Correlation map of (a) MAPI and (d) TCMH. Overlaid SEM image and CLIMSCI correlation decay map (b,c for MAPI and e,f for TCMH) corresponding to a pixel in the marked region in parts a and d. Arrowhead inside the dashed circle indicates the choice of pixel for the correlation decay analysis. Black arrow indicates a pixel from a high correlation region, and corresponding CLIMSCI maps are shown with red background shading. White arrow corresponds to a pixel from the low correlation region, and corresponding CLIMSCI maps are shown with blue background shading. Scale bar is 2 μm.

region or on the same charge cloud, PL intensity traces show a flickering behavior as observed in MAPI.[30] To substantiate such an analogy, we performed simulations involving metastable NRCs of different types and concentrations, as demonstrated in Supporting note 4. At the same experimental conditions, the average PL intensity is twice as large in TCMH compared to MAPI. This can be a result of lower NRC concentration in TCMH. However, it is to be noted that smaller crystals generally emanate higher PL intensity[48] and TCMH grains being smaller in size consist of two grains along the thickness of the sample (Supporting note 1). Therefore, careful analysis is deemed necessary to understand the structure-resolved PL behavior in these samples.

In halide perovskite films, local photophysics has an intriguing relationship with their morphological structure. Considering the contrasting photophysics of MAPI and TCMH films, it is important to understand the role of underlying morphological structures, such as grains and grain boundaries. We therefore performed correlative CLIM and SEM imaging of the same place of the samples. As can be seen from Figure 2a,d, both high and low correlation regions consist of several grains irrespective of the perovskite type. Notably, the theoretical resolution limit of the CLIM correlation map is approximately 400 nm (diffraction limit), which is slightly larger than the size of the grains in both MAPI (280 nm) and TCMH (150 nm).

To find details on the intricate picture of the correlation distribution, we have introduced pixel-based Spatiotemporal Correlation Decay Imaging (CLIMSCI). This allows tracking of how the temporal correlation of a particular pixel changes in space, depicting the decay of correlation or synchronized fluctuation as a function of space (pixels) within a region of interest. When overlaid on SEM images, we can relate these decays of correlation with structure. Figure 2b,c and 2e,f (and Figure S5 and Supporting note 5) show the CLIMSCI maps of pixels corresponding to high correlation (black arrow) and low correlation (white arrow) regions in MAPI and TCMH films, respectively. As can be seen, the correlated domains (0.5 and above) are much larger in MAPI (~1.9 μm in length) than in TCMH (~1.1 μm in length). However, the average number of grains within the 0.5 correlation boundary is similar for both films. These 0.5 correlation boundaries are chosen for the convenience of comparison. Although areas are not circular, these can be approximated to 6−7 grains along the diameter, clearly indicating an effect of the grain boundaries. Another interesting aspect of the CLIMSCI analysis is that the correlation decay is strikingly different for high and low correlation pixels only in TCMH film. While the decay is gradual in high and low correlation regions in MAPI and high correlation pixels in TCMH (Figure 2b,c,e, ~0.05−0.1 unit drop per pixel), correlation drops sharply in the immediate neighboring pixels for low correlation regions in TCMH (Figure 2f, ~0.4 drop in one pixel). Such distinct behavior in TCMH calls for a detailed investigation into the interplay of NRCs and carrier communication.

In the film, the highest correlation regions are the origin of PL fluctuation, and the regions with no fluctuation should exhibit a correlation close to zero. However, a significant correlation around 0.6 ± 0.1 suggests another origin. In TCMH film, sharp decay of correlation in CLIMSCI analysis (Figure 2f) confirms that the PL fluctuations do not originate in this region. Therefore, the fluctuating signals can translate from the surrounding space and get mixed up. To verify this, we have taken an example of comparatively low correlation regions residing in the valley of high correlation regions (Figure 3a). We found that these spatially separated high

https://doi.org/10.1021/cbmi.4c00113
Chem. Biomed. Imaging 2025, 3, 244−252

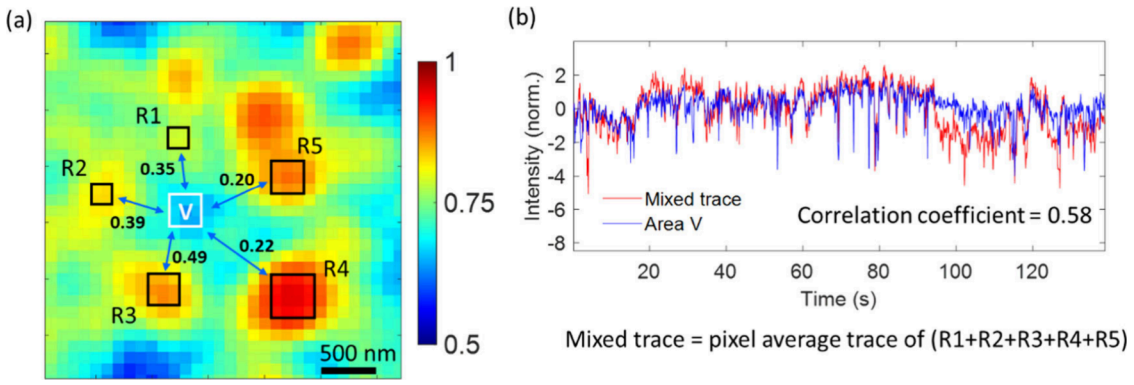

Figure 3. (a) Correlation map of TCMH film demonstrating a low correlation region (V) surrounded by high correlation regions as marked with R1 to R5. Numbers on the arrow indicate the extent of correlation each R-area has with V. (b) Comparison of intensity traces corresponding to area V and mixed signal of areas R1 to R5.

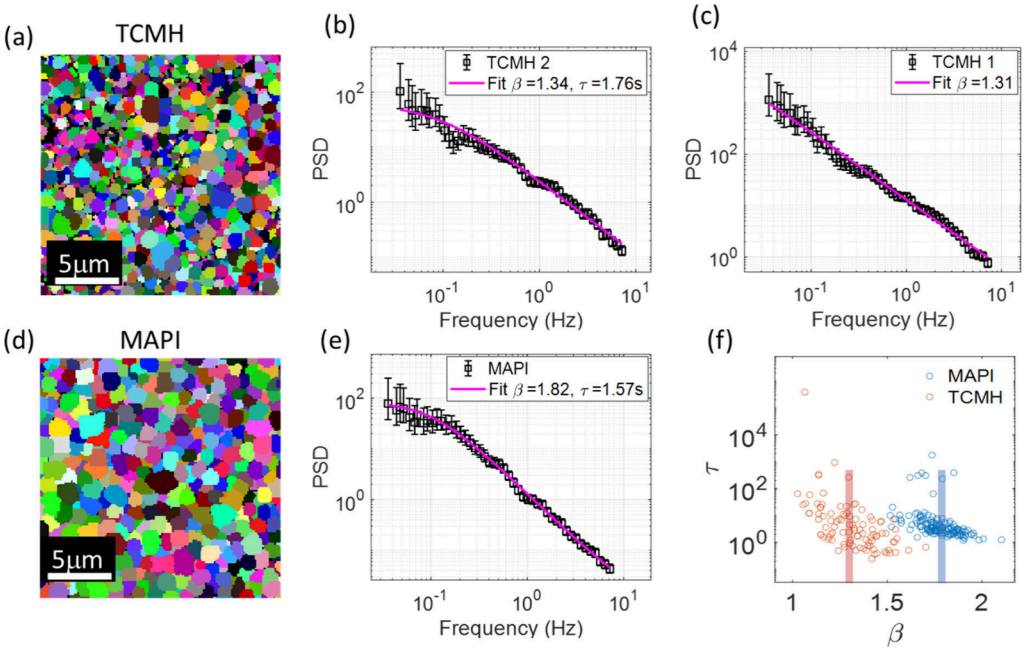

Figure 4. (a,d) CLIM Cluster maps obtained from the same area as shown in Figure 1. (b-e) PSD estimation of intensity traces corresponding to each cluster. PSD of TCMH can be expressed with a Stretched Lorentzian (b) or power-law (c) feature. PSD of MAPI shows only stretched Lorentzian behavior. (f) Statistics of characteristic fluctuation time (τ) and stretching exponent (β).

correlation regions (R1-R5) have different extents of correlation with the valley (V) region. When we combine the pixel averaged traces from these regions as marked with black squares, we found that the mixed trace has a higher correlation (0.58, Figure 3b) with the V area than any of the individual regions (maximum 0.49). One may argue that the tail of the PSF of R1 to R5 extends over the V region; thus, the high correlation arises with the mixed trace. This is, however, unlikely for several reasons. First, the PSF is symmetric, and these regions (R) are asymmetric. Moreover, since the diffraction limit is 400 nm, the full width at half maximum of PSF extends far below 400 nm in each direction from the center. However, the V region is generally 4−7 pixels (400−700 nm) apart from other regions (R1 to R5), thus having such a high correlation (0.58) between mixed trace and trace of V region cannot be accounted by PSF extension alone. Since the thickness of the films and grain size are smaller than the emission wavelength, the resonance effect related to photon reabsorption and/or waveguiding can also be eliminated.

It is well established that halide perovskites possess good electronic and ionic conductivity.[49,50] Previously, we have reported efficient intergrain charge diffusion in mixed cation perovskites (MA/FA) of similar grain size prepared following a similar synthetic protocol.[17] Once the NRCs become active in the high correlation region, it will capture the charge carrier from the vicinity. Consequently, the charges can move toward the NRCs. This motion stops as soon as NRCs become inactive, thus contributing to the fluctuating PL intensity several 100 nm apart from the NRCs location. Therefore, it is fair to conclude that carriers can communicate over at least 500 nm in space from defect free regions to PL quenching NRC regions.

The distinctly different Correlation maps and PL intensity traces of both samples suggest that metastable NRCs in these films are rather different in their fluctuation kinetics and hence also in carrier quenching rates. To identify the local areas where these NRC-induced PL fluctuations are synchronous, we implemented the clustering step of the CLIM method.

https://doi.org/10.1021/cbmi.4c00113
Chem. Biomed. Imaging 2025, 3, 244−252

With a correlation threshold of 0.5, we segmented the correlation map into microscale clusters (Figure 4a, d) which have at least a value of 0.5 correlation among all the pixels. Clusters are considerably larger in MAPI (ca. 2 μm) compared to TCMH (ca. 1 μm). These clusters containing 6−7 grains along diameter match well with the CLIMSCI analysis.

Pixel-averaged intensity traces of individual clusters contain the effect of carrier quenching on the carrier diffusion and radiative recombination. We perform power spectral density (PSD) estimation for a better statistical outlook of the fluctuation events and kinetics of the NRCs. PSD is an effective analytical tool to understand the characteristics of stochastic processes as practiced extensively for noise characterization.[51] Recently this methodology is becoming popular for PL blinking/fluctuation analysis in perovskite systems.[23,39,52] In large nanocrystals (≥100 nm), Auger processes are negligible and PL fluctuations are well explained with the multiple recombination center model.[23,42] Although details can be found elsewhere,[23] in simple terms, when metastable NRCs have a specific rate of switching cycle from active to inactive state, PSD of PL fluctuation takes the shape of a Lorentzian function (eq 1, where β = 2, Materials and methods). When NRCs have a dispersive rate of switching, PSDs tend to become power law with an exponent lower than 2 (eq 2). As shown in Figures 4b, c, and 4e, PSD spectra have distinct shapes for the MAPI and TCMH samples. In MAPI, saturation of PSD at low frequency and power law with a slope close to 2 at high frequency are observed and resemble Lorentzian behavior (Figure 4e). In TCMH, saturation at low frequency is observed only in 30% of cases (Figure 4b). Power-law PSD with an average slope of 1.3 and no apparent saturation at low frequency prevail in this sample (Figure 4c). Although fitting this class of PSDs with a stretched Lorentzian function generally yields longer τ values, we classify it as a power law due to the absence of clear low-frequency saturation.

As we have discussed in detail in our previous studies, the PSD of MAPI is often well described with a stretched Lorentzian function (eq 1) within the multiple recombination center (MRC) model.[23] We extract a characteristic fluctuation time of 1 to 10 s in the present study. This indicates that only one type of NRC is present, with a probability of completing a switching cycle from active to inactive until the next active state within this time window. On the other hand, a slope close to 1 for TCMH suggests dispersive fluctuation kinetics, meaning NRCs causing the PL fluctuations have a switching rate distributed over several orders of magnitude (at least three here, see Supporting note 4 for details). This behavior is quite counterintuitive because MAPI containing a higher NRC density than TCMH is supposed to have a higher possibility for dispersive fluctuation kinetics (Figure S4, Supporting note 4). This fact suggests that PL quenching NRCs are functionally different in these two perovskite compositions.

DISCUSSION

A long carrier diffusion length is one of the main benefactors that accelerated the development of perovskite materials for photovoltaic applications. Carrier diffusion is reported to vary among the perovskite compositions and morphology. It is consistently observed that the diffusion coefficient of charge carriers is larger in MAPI than in TCMH for dimensionally comparable morphologies (e.g., grains or single crystals).[7,31] However, TCMH-based devices often outperform MAPI-based ones in solar cell efficiency.[31,53] This can be understood by considering the interplay of carrier quenching and diffusion linked to the morphological boundaries of the different perovskites.

One may argue whether signal fluctuation originates from closely located metastable NRCs or charge carrier diffusion over space toward a single NRC. When one NRC affects the charge cloud in a local region, it should produce two-level intensity jump time traces. The correlation decay length is determined by charge diffusion and its temporal interaction with the NRC. If the switching of the NRC from active to passive has a specific rate, it should produce a Lorentzian PSD with a slope close to 2. When several such NRCs operate within a local region, the intensity time trace converts to flickering, while the PSD signature remains unchanged. Since such is the behavior for MAPI, correlation decay length is defined by many traps with similar switching rates. In contrast, TCMH time traces, characterized by a few discrete intensity steps and a power-law PSD (slope ∼1.3), suggest that a small number (2−3) of metastable traps with significantly different switching rates influence the local charge cloud and define the correlation decay length.

The present investigation reveals that the extent of communication between nonradiative recombination channels (NRCs) and surrounding photoexcited carriers is larger (in area) in MAPI than in TCMH. Spatially closely located NRCs in MAPI affect the same photogenerated charge cloud. Conversely, in TCMH NRCs are generally located several micrometers apart from each other yet influence charge carriers over a ∼0.5 μm radius. Interestingly, the number of grains involved in this interaction (approximately 6 to 7 grains for 50% correlation decay) is similar for both materials. The larger grain size of MAPI explains the larger correlation domains of this sample compared to TCMH. This fact suggests that grain boundaries rather than the grains themselves act as partial barriers to carrier transport. Notably, these barriers do not fully impede carriers, allowing communication across multiple grains. Moreover, the asymmetric distribution of these domains (evident from CLIMSCI, Figure 2) in both samples suggests the discriminating nature of grain boundaries even within the same film. Importantly, MAPI exhibits a higher concentration of metastable NRCs compared to TCMH (Supporting note 4). In TCMH, the sparse spatial distribution of these NRCs increases the likelihood of charge carrier extraction in device configurations, contributing to their superior photovoltaic performance.

CONCLUSION

We have demonstrated a generic methodology to characterize the local photophysics of perovskite films with CLIM imaging. We further advanced this novel imaging methodology with the modality of CLIMSCI. By integrating scanning electron microscopy with CLIM and CLIMSCI, we establish a robust framework to correlate the nanoscopic structure and functional properties of perovskite samples. Once this structure−function relationship is established for any given perovskite composition and film morphology, CLIM can be applied for the high-throughput optoelectronic characterization of those perovskite thin films. Moreover, our state-of-the-art analysis protocol is arguably very simple and can be seamlessly adapted to the manufacturing line for fast operando device characterization and standardization.

https://doi.org/10.1021/cbmi.4c00113
Chem. Biomed. Imaging 2025, 3, 244−252

MATERIALS AND METHODS

Thin Film Preparation

Perovskite films of $MAPbI_3$ and $(CsPbI_3)_{0.05}(FA_{0.85}MA_{0.15}Pb[I_{0.85}Br_{0.15}]_3)_{0.95}$ were prepared by single-step spin coating technique according to previous reports.[17,47] First, perovskite precursor solutions were prepared by dissolving appropriate materials in DMF: DMSO mixed solution. For the $MAPbI_3$ film, methylammonium iodide (MAI, Sigma-Aldrich) and PbI_2 (TCI) were dissolved at a molar ratio of 1:1 in DMF: DMSO (7:3/v:v) by stirring for 2 h at 60 °C. For the $(CsPbI_3)_{0.05}(FA_{0.85}MA_{0.15}Pb[I_{0.85}Br_{0.15}]_3)_{0.95}$ film, formamidinium iodide (FAI, Sigma-Aldrich), methylammonium bromide (MABr, Sigma-Aldrich), CsI (Sigma-Aldrich), PbI_2 (TCI) and $PbBr_2$ (Sigma-Aldrich) were dissolved at a molar ratio of 0.81:0.14:0.05:0.86:0.14 in DMF: DMSO (5:1/v:v) by stirring for 2 h at 60 °C. Microscope cover glass substrates were carefully cleaned with ethanol, KOH solution and deionized water. To form the films, 150 μL of the precursor solutions were dropped on the glass substrates and spin-coated at 1000 rpm for 10 s, followed by 5000 rpm for 20 s. Ten seconds before the end of the spin coating, 300 μL of ethyl acetate were dropped on the films as antisolvent. After that, the perovskite films were annealed at 100 °C for 40 min, during which the films turned to the brown color typical of perovskite films. The resulting film thickness was on the order of 200 nm, as measured by SEM. All the processes were conducted in air.

Photoluminescence Microscopy Measurements

Fluorescence from perovskite films was analyzed by using an inverted microscope (IX 71, Olympus). Samples were excited with a supercontinuum laser centered at 720 nm, delivering an excitation power of approximately 0.7 W/cm^2 at the microscope stage. Fluorescence was collected via a dry objective lens (UPlanFLN 60×, N.A. 0.95, Olympus) and filtered through a dichroic mirror and long-pass filters. For spectral measurements, the fluorescence signal was dispersed by an imaging spectrograph (CLP-50LD, Bunkou Keiki) equipped with a flipping mirror. This mirror relayed the microscopic image to a CCD camera in the imaging mode, enabling alignment of the emitting spot at the slit center. Upon removing the mirror, fluorescence passing through the vertical slit was spectrally dispersed, providing the local fluorescence spectrum at the film's vertical position. An electron-multiplying CCD camera (iXon, Andor Technology) detected the fluorescence with exposure times of 30 ms for blinking and 50 ms for spectral measurements.

Scanning Electron Microscopy Imaging

Structural characterization of the MHP films was performed by JSM-7500F (JEOL) field emission scanning electron microscope with an accelerating voltage of 6.0 kV. The samples were fixed to the base with carbon tape and treated with Osmium plasma for conductive layer coating. Thickness of the samples was measured by cross-sectioning the films.

CLIM Imaging

To generate correlation maps and cluster maps, we employed the CLIM software described previously.[30] In brief, CLIM analyzes the temporal intensity traces of pixels in an image. It first calculates the Pearson correlation coefficient over time between the intensity trace of each pixel and those of its eight immediate neighbors. The correlation map is then obtained by averaging these eight correlation values for each pixel and mapping the result, producing an image with correlation-based contrast. For the cluster map, CLIM applies a self-optimized correlation threshold to group pixels with significant correlations, effectively identifying regions with similar temporal behavior.

Power Spectral Density Analysis of the Intensity Traces

Power spectral density estimation is well documented in previously published papers.[23,39,54] The code is available on the following webpage (10.5281/zenodo.8027381). The PSDs in this article are fitted with the equations for a stretched Lorentzian (as described by eq 1) and a power-law (as described by eq 2).

$$\mathrm{PSD}(f) = \frac{A}{1 + (f/f_0)^{\beta}} \tag{1}$$

$$\mathrm{PSD}(f) = \frac{A'}{f^{\beta}} \tag{2}$$

Here $f_0 = 1/(2\pi\tau)$ and τ is the characteristic fluctuation time. β is the stretching exponent, equal to 2 for fluctuations caused by one or several two-level systems with the same characteristic frequency. When multiple two-level systems of variable fluctuation times (several orders of magnitude) participate the stretching exponent diminishes and transforms to power law.

ASSOCIATED CONTENT

Supporting Information

The Supporting Information is available free of charge at https://pubs.acs.org/doi/10.1021/cbmi.4c00113.

SEM images of the perovskite thin films, absorption and emission spectra, simulated intensity time traces, overlaid SEM and CLIMSCI images (PDF)

Supporting movie 1_MAPI: a widefield photoluminescence microscopy movie that is used to generate CLIM maps and figures (AVI)

Supporting movie 2_TCMH: a widefield photoluminescence microscopy movie that is used to generate CLIM maps and figures (AVI)

AUTHOR INFORMATION

Corresponding Authors

Sudipta Seth − *Laboratory for Photochemistry and Spectroscopy, Division for Molecular Imaging and Photonics, Department of Chemistry, Katholieke Universiteit Leuven, Leuven 3001, Belgium;* orcid.org/0000-0002-8666-4080; Email: sudipta.seth@kuleuven.be

Martin Vacha − *Department of Materials Science and Engineering, Tokyo Institute of Technology, Meguro-ku, Tokyo 152-8552, Japan;* orcid.org/0000-0002-5729-9774; Email: vacha.m.aa@m.titech.ac.jp

Johan Hofkens − *Laboratory for Photochemistry and Spectroscopy, Division for Molecular Imaging and Photonics, Department of Chemistry, Katholieke Universiteit Leuven, Leuven 3001, Belgium; Max Planck Institute for Polymer Research, Mainz 55128, Germany;* orcid.org/0000-0002-9101-0567; Email: johan.hofkens@kuleuven.be

Authors

Boris Louis − *Laboratory for Photochemistry and Spectroscopy, Division for Molecular Imaging and Photonics, Department of Chemistry, Katholieke Universiteit Leuven, Leuven 3001, Belgium*

Koki Asano − *Department of Materials Science and Engineering, Tokyo Institute of Technology, Meguro-ku, Tokyo 152-8552, Japan*

Toon Van Roy − *Laboratory for Photochemistry and Spectroscopy, Division for Molecular Imaging and Photonics, Department of Chemistry, Katholieke Universiteit Leuven, Leuven 3001, Belgium;* orcid.org/0009-0005-5370-695X

Maarten B. J. Roeffaers − *Laboratory for Photochemistry and Spectroscopy, Division for Molecular Imaging and Photonics, Department of Chemistry, Katholieke Universiteit Leuven, Leuven 3001, Belgium;* orcid.org/0000-0001-6582-6514

Elke Debroye − *Laboratory for Photochemistry and Spectroscopy, Division for Molecular Imaging and Photonics,*

Department of Chemistry, Katholieke Universiteit Leuven, Leuven 3001, Belgium; orcid.org/0000-0003-1087-4759
Ivan G. Scheblykin − *Division of Chemical Physics and NanoLund, Lund University, Lund 22100, Sweden;* orcid.org/0000-0001-6059-4777

Complete contact information is available at: https://pubs.acs.org/10.1021/cbmi.4c00113

Notes

The authors declare no competing financial interest.

■ ACKNOWLEDGMENTS

S.S. acknowledges the support of Marie Skłodowska-Curie postdoctoral fellowship (No. 101151427, SPS_Nano) from the European Union's Horizon Europe program, short stay abroad grant (K257023N) and travel grant (K147824N) from Research Foundation-Flanders (FWO). B.L. thanks FWO for his Junior Postdoctoral fellowship (12AGZ24N). E.D. acknowledges funding from the KU Leuven Internal Funds (grant numbers C14/23/090 and CELSA/23/018), the Research Foundation-Flanders (FWO, grant number G0AHQ25N) and the European Union (ERC Starting Grant, 101117274 X-PECT). However, the views and opinions expressed are those of the authors only and do not necessarily reflect those of the European Union or European Research Council. Neither the European Union nor the granting authority can be held responsible for them. J.H. acknowledges financial support from the Research Foundation-Flanders (FWO, Grant Nos. G098319N, G0F2322N, S002019N, VS06523N, G0AHQ25N) from the Flemish government through long-term structural funding Methusalem (CASAS2, Meth/15/04), and the MPIP as MPI fellow. M.V. acknowledges financial support by the JSPS KAKENHI grant number 24K01449 and by the JSPS KAKENHI grant number 23H04875 in Grant-in-Aid for Transformative Research Areas 'Materials Science of Meso-Hierarchy'.

■ REFERENCES

(1) *National Renewable Energy Laboratory. Best Research-Cell Efficiency Chart | Photovoltaic Research | NREL.* https://www.nrel.gov/pv/cell-efficiency.html.
(2) Wang, Z.; Shan, C.; Liu, C.; Tang, X.; Luo, D.; Tang, H.; Song, Z.; Wang, J.; Ren, Z.; Ma, J.; Wang, H.; Sun, J.; Zhang, N.; Choy, W. C. H.; Liu, Y.; Kyaw, A. K. K.; Sun, X. W.; Wu, D.; Wang, K. In Situ Growth of Perovskite Single-Crystal Thin Films with Low Trap Density. *Cell Rep. Phys. Sci.* **2023**, *4* (4), No. 101363.
(3) Jin, H.; Debroye, E.; Keshavarz, M.; Scheblykin, I. G.; Roeffaers, M. B. J.; Hofkens, J.; Steele, J. A. It's a Trap! On the Nature of Localised States and Charge Trapping in Lead Halide Perovskites. *Mater. Horiz.* **2020**, *7* (2), 397−410.
(4) Ahn, N.; Kwak, K.; Jang, M. S.; Yoon, H.; Lee, B. Y.; Lee, J.-K.; Pikhitsa, P. V.; Byun, J.; Choi, M. Trapped Charge-Driven Degradation of Perovskite Solar Cells. *Nat. Commun.* **2016**, *7*, 13422.
(5) Zhang, D.; Li, D.; Hu, Y.; Mei, A.; Han, H. Degradation Pathways in Perovskite Solar Cells and How to Meet International Standards. *Commun. Mater.* **2022**, *3* (1), 58.
(6) Stranks, S. D.; Eperon, G. E.; Grancini, G.; Menelaou, C.; Alcocer, M. J. P.; Leijtens, T.; Herz, L. M.; Petrozza, A.; Snaith, H. J. Electron-Hole Diffusion Lengths Exceeding 1 Micrometer in an Organometal Trihalide Perovskite Absorber. *Science* **2013**, *342* (6156), 341−344.
(7) Saidaminov, M. I.; Williams, K.; Wei, M.; Johnston, A.; Quintero-Bermudez, R.; Vafaie, M.; Pina, J. M.; Proppe, A. H.; Hou, Y.; Walters, G.; Kelley, S. O.; Tisdale, W. A.; Sargent, E. H. Multi-Cation Perovskites Prevent Carrier Reflection from Grain Surfaces. *Nat. Mater.* **2020**, *19* (4), 412−418.
(8) Yuan, Y.; Yan, G.; Dreessen, C.; Rudolph, T.; Hülsbeck, M.; Klingebiel, B.; Ye, J.; Rau, U.; Kirchartz, T. Shallow Defects and Variable Photoluminescence Decay Times up to 280 Ms in Triple-Cation Perovskites. *Nat. Mater.* **2024**, *23* (3), 391−397.
(9) Delport, G.; Macpherson, S.; Stranks, S. D. Imaging Carrier Transport Properties in Halide Perovskites Using Time-Resolved Optical Microscopy. *Adv. Energy Mater.* **2020**, *10* (26), No. 1903814.
(10) Zhang, H.; Debroye, E.; Vina-Bausa, B.; Valli, D.; Fu, S.; Zheng, W.; Di Virgilio, L.; Gao, L.; Frost, J. M.; Walsh, A.; Hofkens, J.; Wang, H. I.; Bonn, M. Stable Mott Polaron State Limits the Charge Density in Lead Halide Perovskites. *ACS Energy Lett.* **2023**, *8* (1), 420−428.
(11) Zhang, H.; Debroye, E.; Steele, J. A.; Roeffaers, M. B. J.; Hofkens, J.; Wang, H. I.; Bonn, M. Highly Mobile Large Polarons in Black Phase $CsPbI_3$. *ACS Energy Lett.* **2021**, *6* (2), 568−573.
(12) Tennyson, E. M.; Doherty, T. A. S.; Stranks, S. D. Heterogeneity at Multiple Length Scales in Halide Perovskite Semiconductors. *Nat. Rev. Mater.* **2019**, *4* (9), 573−587.
(13) Stranks, S. D. Multimodal Microscopy Characterization of Halide Perovskite Semiconductors: Revealing a New World (Dis)-Order. *Matter* **2021**, *4* (12), 3852−3866.
(14) De Quilettes, D. W.; Vorpahl, S. M.; Stranks, S. D.; Nagaoka, H.; Eperon, G. E.; Ziffer, M. E.; Snaith, H. J.; Ginger, D. S. Impact of Microstructure on Local Carrier Lifetime in Perovskite Solar Cells. *Science* **2015**, *348* (6235), 683−686.
(15) Jariwala, S.; Sun, H.; Adhyaksa, G. W. P.; Lof, A.; Muscarella, L. A.; Ehrler, B.; Garnett, E. C.; Ginger, D. S. Local Crystal Misorientation Influences Non-Radiative Recombination in Halide Perovskites. *Joule* **2019**, *3* (12), 3048−3060.
(16) Yuan, H.; Debroye, E.; Janssen, K.; Naiki, H.; Steuwe, C.; Lu, G.; Moris, M.; Orgiu, E.; Uji-i, H.; De Schryver, F.; Samorì, P.; Hofkens, J.; Roeffaers, M. Degradation of Methylammonium Lead Iodide Perovskite Structures through Light and Electron Beam Driven Ion Migration. *J. Phys. Chem. Lett.* **2016**, *7* (3), 561−566.
(17) Agarwal, A.; Omagari, S.; Vacha, M. Nanoscale Structural Heterogeneity and Efficient Intergrain Charge Diffusion in a Series of Mixed MA/FA Halide Perovskite Films. *ACS Energy Lett.* **2022**, *7* (8), 2443−2449.
(18) Yuan, H.; Debroye, E.; Bladt, E.; Lu, G.; Keshavarz, M.; Janssen, K. P. F.; Roeffaers, M. B. J.; Bals, S.; Sargent, E. H.; Hofkens, J. Imaging Heterogeneously Distributed Photo-Active Traps in Perovskite Single Crystals. *Adv. Mater.* **2018**, *30* (13), No. 1705494.
(19) Doherty, T. A. S.; Winchester, A. J.; Macpherson, S.; Johnstone, D. N.; Pareek, V.; Tennyson, E. M.; Kosar, S.; Kosasih, F. U.; Anaya, M.; Abdi-Jalebi, M.; Andaji-Garmaroudi, Z.; Wong, E. L.; Madéo, J.; Chiang, Y.-H.; Park, J.-S.; Jung, Y.-K.; Petoukhoff, C. E.; Divitini, G.; Man, M. K. L.; Ducati, C.; Walsh, A.; Midgley, P. A.; Dani, K. M.; Stranks, S. D. Performance-Limiting Nanoscale Trap Clusters at Grain Junctions in Halide Perovskites. *Nature* **2020**, *580* (7803), 360−366.
(20) Qin, T.-X.; You, E.-M.; Zhang, M.-X.; Zheng, P.; Huang, X.-F.; Ding, S.-Y.; Mao, B.-W.; Tian, Z.-Q. Quantification of Electron Accumulation at Grain Boundaries in Perovskite Polycrystalline Films by Correlative Infrared-Spectroscopic Nanoimaging and Kelvin Probe Force Microscopy. *Light Sci. Appl.* **2021**, *10* (1), 84.
(21) Frohna, K.; Anaya, M.; Macpherson, S.; Sung, J.; Doherty, T. A. S.; Chiang, Y.-H.; Winchester, A. J.; Orr, K. W. P.; Parker, J. E.; Quinn, P. D.; Dani, K. M.; Rao, A.; Stranks, S. D. Nanoscale Chemical Heterogeneity Dominates the Optoelectronic Response of Alloyed Perovskite Solar Cells. *Nat. Nanotechnol.* **2022**, *17* (2), 190−196.
(22) Feldmann, S.; Macpherson, S.; Senanayak, S. P.; Abdi-Jalebi, M.; Rivett, J. P. H.; Nan, G.; Tainter, G. D.; Doherty, T. A. S.; Frohna, K.; Ringe, E.; Friend, R. H.; Sirringhaus, H.; Saliba, M.; Beljonne, D.; Stranks, S. D.; Deschler, F. Photodoping through Local Charge Carrier Accumulation in Alloyed Hybrid Perovskites for Highly Efficient Luminescence. *Nat. Photonics* **2020**, *14* (2), 123−128.
(23) Seth, S.; Podshivaylov, E. A.; Li, J.; Gerhard, M.; Kiligaridis, A.; Frantsuzov, P. A.; Scheblykin, I. G. Presence of Maximal Character-

istic Time in Photoluminescence Blinking of $MAPbI_3$ Perovskite. *Adv. Energy Mater.* **2021**, *11* (44), No. 2102449.
(24) Merdasa, A.; Tian, Y.; Camacho, R.; Dobrovolsky, A.; Debroye, E.; Unger, E. L.; Hofkens, J.; Sundström, V.; Scheblykin, I. G. "Supertrap" at Work: Extremely Efficient Nonradiative Recombination Channels in $MAPbI_3$ Perovskites Revealed by Luminescence Super-Resolution Imaging and Spectroscopy. *ACS Nano* **2017**, *11* (6), 5391−5404.
(25) Sharma, D. K.; Hirata, S.; Vacha, M. Single-Particle Electroluminescence of CsPbBr3 Perovskite Nanocrystals Reveals Particle-Selective Recombination and Blinking as Key Efficiency Factors. *Nat. Commun.* **2019**, *10* (1), 4499.
(26) Bhagyalakshmi, S. B.; Zhang, D.; Biju, V. Electroluminescence of Halide Perovskite Single Crystals Showing Stochastically Active Multiple Emitting Centers. *J. Phys. Chem. C* **2022**, *126* (42), 17826−17835.
(27) Garrett, J. L.; Tennyson, E. M.; Hu, M.; Huang, J.; Munday, J. N.; Leite, M. S. Real-Time Nanoscale Open-Circuit Voltage Dynamics of Perovskite Solar Cells. *Nano Lett.* **2017**, *17* (4), 2554−2560.
(28) Tennyson, E. M.; Howard, J. M.; Roose, B.; Garrett, J. L.; Munday, J. N.; Abate, A.; Leite, M. S. The Effects of Incident Photon Energy on the Time-Dependent Voltage Response of Lead Halide Perovskites. *Chem. Mater.* **2019**, *31* (21), 8969−8976.
(29) Seth, S.; Mondal, N.; Patra, S.; Samanta, A. Fluorescence Blinking and Photoactivation of All-Inorganic Perovskite Nanocrystals $CsPbBr_3$ and $CsPbBr_2$ I. *J. Phys. Chem. Lett.* **2016**, *7* (2), 266−271.
(30) Louis, B.; Seth, S.; An, Q.; Ji, R.; Vaynzof, Y.; Hofkens, J.; Scheblykin, I. G. In Operando Locally-Resolved Photophysics in Perovskite Solar Cells by Correlation Clustering Imaging. *Adv. Mater.* **2024**, No. 2413126.
(31) Saliba, M.; Matsui, T.; Seo, J.-Y.; Domanski, K.; Correa-Baena, J.-P.; Nazeeruddin, M. K.; Zakeeruddin, S. M.; Tress, W.; Abate, A.; Hagfeldt, A.; Grätzel, M. Cesium-Containing Triple Cation Perovskite Solar Cells: Improved Stability, Reproducibility and High Efficiency. *Energy Environ. Sci.* **2016**, *9* (6), 1989−1997.
(32) Moerner, W. E. Those Blinking Single Molecules. *Science* **1997**, *277* (5329), 1059−1060.
(33) Clifford, J. N.; Bell, T. D. M.; Tinnefeld, P.; Heilemann, M.; Melnikov, S. M.; Hotta, J.; Sliwa, M.; Dedecker, P.; Sauer, M.; Hofkens, J.; Yeow, E. K. L. Fluorescence of Single Molecules in Polymer Films: Sensitivity of Blinking to Local Environment. *J. Phys. Chem. B* **2007**, *111* (25), 6987−6991.
(34) Efros, A. L.; Nesbitt, D. J. Origin and Control of Blinking in Quantum Dots. *Nat. Nanotechnol.* **2016**, *11* (8), 661−671.
(35) Yuan, G.; Gómez, D. E.; Kirkwood, N.; Boldt, K.; Mulvaney, P. Two Mechanisms Determine Quantum Dot Blinking. *ACS Nano* **2018**, *12* (4), 3397−3405.
(36) Jin, H.; Steele, J. A.; Cheng, R.; Parveen, N.; Roeffaers, M. B. J.; Hofkens, J.; Debroye, E. Experimental Evidence of Chloride-Induced Trap Passivation in Lead Halide Perovskites through Single Particle Blinking Studies. *Adv. Opt. Mater.* **2021**, *9* (23), No. 2002240.
(37) Jin, H.; Mukherjee, A.; Chouhan, L.; Steele, J. A.; De Jong, F.; Gao, Y.; Roeffaers, M. B. J.; Hofkens, J.; Debroye, E. Single-Particle Optical Study on the Effect of Chloride Post-Treatment of $MAPbI_3$ Nano/Microcrystals. *Nanoscale* **2023**, *15* (11), 5437−5447.
(38) Dertinger, T.; Colyer, R.; Iyer, G.; Weiss, S.; Enderlein, J. Fast, Background-Free, 3D Super-Resolution Optical Fluctuation Imaging (SOFI). *Proc. Natl. Acad. Sci. U. S. A.* **2009**, *106* (52), 22287−22292.
(39) Frantsuzov, P. A.; Volkán-Kacsó, S.; Jankó, B. Universality of the Fluorescence Intermittency in Nanoscale Systems: Experiment and Theory. *Nano Lett.* **2013**, *13* (2), 402−408.
(40) Tian, Y.; Merdasa, A.; Peter, M.; Abdellah, M.; Zheng, K.; Ponseca, C. S.; Pullerits, T.; Yartsev, A.; Sundström, V.; Scheblykin, I. G. Giant Photoluminescence Blinking of Perovskite Nanocrystals Reveals Single-Trap Control of Luminescence. *Nano Lett.* **2015**, *15* (3), 1603−1608.
(41) Yuan, H.; Debroye, E.; Caliandro, G.; Janssen, K. P. F.; Van Loon, J.; Kirschhock, C. E. A.; Martens, J. A.; Hofkens, J.; Roeffaers, M. B. J. Photoluminescence Blinking of Single-Crystal Methylammonium Lead Iodide Perovskite Nanorods Induced by Surface Traps. *ACS Omega* **2016**, *1* (1), 148−159.
(42) Eremchev, I. Yu.; Tarasevich, A. O.; Li, J.; Naumov, A. V.; Scheblykin, I. G. Lack of Photon Antibunching Supports Supertrap Model of Photoluminescence Blinking in Perovskite Sub-Micrometer Crystals. *Adv. Opt. Mater.* **2021**, *9* (3), No. 2001596.
(43) Louis, B.; Seth, S.; An, Q.; Ji, R.; Vaynzof, Y.; Hofkens, J.; Scheblykin, I. Correlation Clustering Imaging: A Method for Functional Mapping of Semiconductor Materials and Photovoltaic Devices in Operando. *ChemRxiv*, March 8, 2024. DOI: 10.26434/chemrxiv-2024-76908.
(44) Pearson, K. Note on Regression and Inheritance in the Case of Two Parents. *Proc. R. Soc. London Ser. I* **1895**, *58*, 240−242.
(45) Kolin, D. L.; Wiseman, P. W. Advances in Image Correlation Spectroscopy: Measuring Number Densities, Aggregation States, and Dynamics of Fluorescently Labeled Macromolecules in Cells. *Cell Biochem. Biophys.* **2007**, *49* (3), 141−164.
(46) Wiseman, P. W. Image Correlation Spectroscopy: Principles and Applications. *Cold Spring Harb Protoc.* **2015**, *4*, 336.
(47) Zhao, R.; Wang, L.; Huang, J.; Miao, X.; Sun, L.; Hua, Y.; Wang, Y. Amino-Capped Zinc Oxide Modified Tin Oxide Electron Transport Layer for Efficient Perovskite Solar Cells. *Cell Rep. Phys. Sci.* **2021**, *2* (10), No. 100590.
(48) Brenes, R.; Guo, D.; Osherov, A.; Noel, N. K.; Eames, C.; Hutter, E. M.; Pathak, S. K.; Niroui, F.; Friend, R. H.; Islam, M. S.; Snaith, H. J.; Bulović, V.; Savenije, T. J.; Stranks, S. D. Metal Halide Perovskite Polycrystalline Films Exhibiting Properties of Single Crystals. *Joule* **2017**, *1* (1), 155−167.
(49) Guo, Y.; Yin, X.; Liu, D.; Liu, J.; Zhang, C.; Xie, H.; Yang, Y.; Que, W. Photoinduced Self-Healing of Halide Segregation in Mixed-Halide Perovskites. *ACS Energy Lett.* **2021**, *6* (7), 2502−2511.
(50) Sun, Q.; Zhang, X.; Zhao, C.; Tian, W.; Jin, S. Carrier Transport in Lead Halide Perovskites. *J. Phys. Chem. C* **2023**, *127*, 22868−22879.
(51) Weissman, M. B. 1 f Noise and Other Slow, Nonexponential Kinetics in Condensed Matter. *Rev. Mod. Phys.* **1988**, *60* (2), 537−571.
(52) Praneeth, N. V. S.; Akhil, S.; Mukherjee, A.; Seth, S.; Khatua, S.; Mishra, N. Amine-Free Multi-Faceted $CsPbBr_3$ Nanocrystals for Complete Suppression of Long-Lived Dark States. *Adv. Opt. Mater.* **2024**, *12* (16), No. 2303222.
(53) Liu, S.; Biju, V. P.; Qi, Y.; Chen, W.; Liu, Z. Recent Progress in the Development of High-Efficiency Inverted Perovskite Solar Cells. *NPG Asia Mater.* **2023**, *15* (1), 27.
(54) Podshivaylov, E. A.; Kniazeva, M. A.; Tarasevich, A. O.; Eremchev, I. Yu.; Naumov, A. V.; Frantsuzov, P. A. A Quantitative Model of Multi-Scale Single Quantum Dot Blinking. *J. Mater. Chem. C* **2023**, *11*, 8570−8576.